Title

Tunable Biogenic Manganese Oxides

Journal

Chemistry - A European Journal, 23(54)

ISSN

0947-6539

Authors

Simonov, Alexandr N
Hocking, Rosalie K
Tao, Lizhi
et al.

Publication Date

2017-09-27

DOI

10.1002/chem.201702579

Peer reviewed

ChemPubSoc Europe

DOI: 10.1002/chem.201702579

CHEMISTRY A European Journal Full Paper

Biogenic Materials

Tunable Biogenic Manganese Oxides

Alexandr N. Simonov,*[a] Rosalie K. Hocking,[b] Lizhi Tao,[c] Thomas Gengenbach,[d] Timothy Williams,[e] Xi-Ya Fang,[e] Hannah J. King,[b] Shannon A. Bonke,[a] Dijon A. Hoogeveen,[a] Christine A. Romano,[f] Bradley M. Tebo,[f] Lisandra L. Martin,[a] William H. Casey,*[c, g] and Leone Spiccia[a]

To the deepest sorrow of the co-authors, Professor Leone Spiccia - an outstanding scientist and personality, passed away untimely before this work, which was inspired by him, could be published. This work is dedicated to the memory of our good friend Leone.

Abstract: Influence of the conditions for aerobic oxidation of $Mn^{2+}_{(aq)}$ catalysed by the MnxEFG protein complex on the morphology, structure and reactivity of the resulting biogenic manganese oxides (MnO_x) is explored. Physical characterisation of MnO_x includes scanning and transmission electron microscopy, and X-ray photoelectron and K-edge Mn, Fe X-ray absorption spectroscopy. This characterisation reveals that the MnO_x materials share the structural features of birnessite, yet differ in the degree of structural disorder. Importantly, these biogenic products exhibit strikingly different morphologies that can be easily controlled. Changing the substrate-to-protein ratio produces MnO_x either as nm-thin sheets, or rods with diameters below 20 nm, or a combination of the two. Mineralisation in solutions that contain $Fe^{2+}_{(aq)}$ makes solids with significant disorder in the structure, while the presence of $Ca^{2+}_{(aq)}$ facilitates formation of more ordered materials. The (photo)oxidation and (photo)electrocatalytic capacity of the MnO_x minerals is examined and correlated with their structural properties.

Introduction

Naturally occurring and artificially synthesised manganese oxides (MnO_x) deservedly receive massive investigative attention. These materials are even given specific names like "scavengers of the sea"[1] or "catalytic Swiss army knife"[2] to emphasise their significance to the environment and technology. The role of the MnO_x minerals in nature includes degradation of organic compounds,[3] as well as the oxidation and sorption of metals and metalloids.[4] The structural and redox versatility of manganese oxide solids, and their capacity to incorporate other elements, make them useful for a wide range of applications, for example, as selective oxidation catalysts for organic synthesis, electrocatalysts for the oxygen evolution and reduction reactions, electrode materials for supercapacitors and batteries, and even as magnetic-resonance contrast agents for brain studies. A comprehensive picture of the utility of manganese oxides for chemical, physical and biological technologies is available from a recent review by Najafpour and co-authors[2] and references therein.

The geochemical manganese cycle is dominated by mineralisation of MnO_x solids followed by reduction with the formation of dissolved $Mn^{2+}_{(aq)}$. This occurs in the photic zone of the ocean[5] in which the predominant formation pathway is the diurnal microbial oxidation of $Mn^{2+}_{(aq)}$ to MnO_x by molecular oxygen.[3b] It is also prevalent at oxic–anoxic interfaces that occur in stratified water bodies and aquatic sediments.[6] There is extensive evidence that enzymes like animal heme peroxidases[7]

[a] Dr. A. N. Simonov, Dr. S. A. Bonke, D. A. Hoogeveen, Prof. L. L. Martin, Prof. L. Spiccia
School of Chemistry and
the ARC Centre of Excellence for Electromaterials Science
Monash University, Victoria 3800 (Australia)
E-mail: alexandr.simonov@monash.edu

[b] Dr. R. K. Hocking, H. J. King
Discipline of Chemistry, College of Science and Engineering
James Cook University, Queensland 4811 (Australia)

[c] L. Tao, Prof. W. H. Casey
Department of Chemistry, University of California
One Shields Avenue, Davis, California 95616 (USA)

[d] Dr. T. Gengenbach
Commonwealth Scientific and
Industrial Research Organisation Manufacturing Flagship
Clayton, Victoria 3168 (Australia)

[e] Dr. T. Williams, Dr. X.-Y. Fang
Monash Centre for Electron Microscopy
Monash University, Victoria, 3800 (Australia)

[f] Dr. C. A. Romano, Prof. B. M. Tebo
Division of Environmental and Biomolecular Systems
Institute of Environmental Health
Oregon Health & Science University
Portland, Oregon 97239 (USA)

[g] Prof. W. H. Casey
Department of Earth and Planetary Sciences
University of California
One Shields Avenue, Davis, California 95616 (USA)
E-mail: whcasey@ucdavis.edu

Supporting information and the ORCID identification number(s) for the author(s) of this article can be found under https://doi.org/10.1002/chem.201702579.

and multicopper oxidases[8] catalyse the oxidation of $Mn^{2+}_{(aq)}$ by dissolved O_2. One of these MnO_x-producing enzymes, MnxG, was recently isolated in an active form as a part of the MnxEFG protein complex from a marine *Bacillus* species strain PL-12.[8a] The MnxG-catalysed oxidation of $Mn^{2+}_{(aq)}$ uses O_2 as the terminal electron acceptor and was probed by electron paramagnetic resonance spectroscopy.[8b] These authors concluded that the enzymatic mechanism is similar to that by which multicopper oxidases catalyse oxidation of organic compounds.[9] Briefly, Type 1 "blue" copper sites oxidise $Mn^{2+}_{(aq)}$ to $Mn^{3+}_{(aq)}$ and $Mn^{3+}_{(aq)}$ to $Mn^{4+}_{(aq)}$,[8a,10] and extracted electrons are then transferred to the tandem triangular site composed of type 2 "normal" copper and type 3 "coupled binuclear" copper, in which O_2 is reduced to water (Scheme 1). The freshly produced $Mn^{3+}_{(aq)}$ and $Mn^{4+}_{(aq)}$ species undergo fast hydrolysis and polymerisation to form MnO_x solids under natural pH conditions.

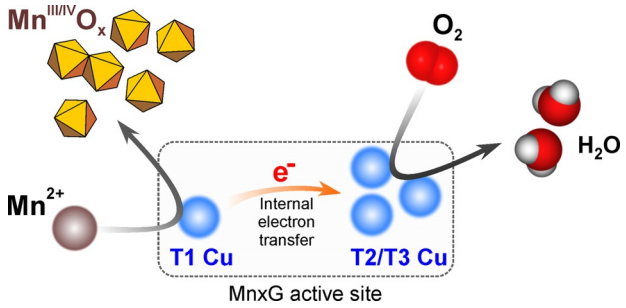

Scheme 1. A plausible mechanism of MnO_x mineralisation catalysed by MnxG.

Manganese oxide solids produced by the MnxG-containing marine *Bacillus* spores and the MnxEFG protein complex under various conditions were previously studied to determine their structure and the electronic state of manganese.[8a,11] The kinetics of the MnO_x mineralisation as catalysed by the marine *Bacillus* spores was also analysed in detail by Toyoda and Tebo.[10b,12] Temperature, pH, Mn^{2+} concentration, ionic strength and the presence of some non-manganese ions were found to influence the structure of the products and the rates of formation of the MnO_x minerals, as might be expected. Initial X-ray diffraction (XRD) studies demonstrated the capacity of the marine *Bacillus* spores to catalyse oxidation of $Mn^{2+}_{(aq)}$ to Mn^{IV}-containing minerals when the substrate is present at comparatively low concentrations in solution.[11a] Increasing the concentration of $Mn^{2+}_{(aq)}$ resulted in predominant precipitation of the Mn^{III}-based solids. Further detailed insights into the mechanism of formation and structure of the biogenic MnO_x minerals were obtained mainly through X-ray absorption spectroscopic (XAS) techniques. These studies provided consistent evidence that the major product of the aerobic $Mn^{2+}_{(aq)}$ oxidation catalysed by marine *Bacillus* spores and the MnxEFG protein complex (with $c_{Mn(II)}$:c_{MnxEFG} molar ratio of about 4.5×10^5) in solutions containing NaCl exhibits the features of δ-MnO_2 and hexagonal birnessites at near-neutral pH, with the average oxidation state of manganese between 3.7 and 4.0.[8a,11d] The presence of Ca^{2+} in solutions significantly enhances the rate of mineralisation by the *Bacillus* spores[10b] and results in MnO_x with a lower average oxidation state (3.5–3.7) and improved long-range order.[11e] The structural features of these minerals resemble those of triclinic or orthogonal phyllomanganates. A qualitatively similar effect was found when mineralisation was catalysed by low concentrations of the purified MnxEFG protein complex ($c_{Mn(II)}$:c_{MnxEFG} molar ratio of about 4.5×10^6).[8a]

Previous studies mainly focused on the mineralisation conditions that are close to those of natural settings, which is evidently important for understanding the geochemical Mn cycle. The recent success in isolation of the MnO_x-producing enzyme, namely, the MnxEFG protein complex, in an active form that is stable under a variety of laboratory conditions[8a,13] now provides an opportunity for facile synthesis of manganese oxides with unusual characteristics for applied purposes. The present work aims to explore such possibilities, in particular, by using comparatively high concentrations of the $Mn^{2+}_{(aq)}$ substrate with low $c_{Mn(II)}$:$c_{MnxEFG} \leq 1.0\times10^5$ and by undertaking mineralisation in the presence of dissolved $Fe^{2+}_{(aq)}$ and also large amounts of the $Ca^{2+}_{(aq)}$ species.

Results and Discussion

Morphological variety

Upon addition of (sub)mM concentrations of $Mn^{2+}_{(aq)}$ to a transparent and colourless 20 nM MnxEFG solution in 10 mM HEPES + 50 mM NaCl (pH 7.8), the colour of the mixture changed progressively to yellow and then to dark brown, indicating the formation of the suspended, highly dispersed MnO_x solids (Figure 1). The time needed to achieve the sustained deep brown colouration of the MnO_x dispersions serves as a qualitative indication of the completion of the reaction and depends, sensitively, on the initial composition of the solution. In

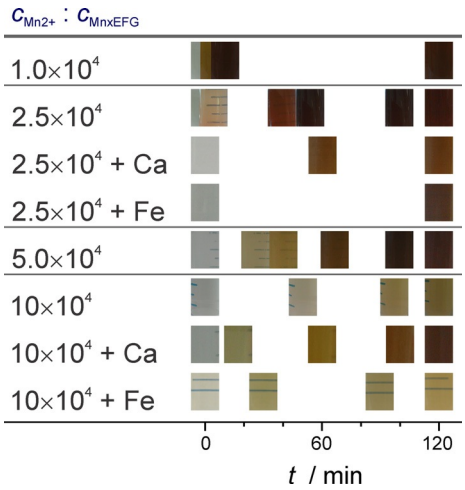

Figure 1. Photographs of the 20 nM MnxEFG solutions (10 mM HEPES + 50 mM NaCl, pH 7.8) taken after adding different amounts of $Mn^{2+}_{(aq)}$ (molar $c_{Mn(II)}$:c_{MnxEFG} ratios are shown on the left). The solutions were left undisturbed in closed vials for an equal amount of time. In some cases, $Ca^{2+}_{(aq)}$ and $Fe^{2+}_{(aq)}$ were also present in solutions (concentrations are provided in Figures 2 and 3).

particular, decreasing the molar ratio of $c_{Mn(II)}$:$c_{MnxEFGaq)}$ from 10×10^4 ($c_{Mn(II)}=2$ mM) to 1.0×10^4 ($c_{Mn(II)}=0.2$ mM) apparently enhances the rate of mineralisation, as does the introduction of $Ca^{2+}_{(aq)}$ (with $c_{Mn(II)}$:$c_{MnxEFG}=10\times10^4$) in accord with previous reports[10b, 13b] (Figure 1).

Interestingly, the Ca^{2+}-free dispersion with $c_{Mn(II)}$:$c_{MnxEFG}=10\times10^4$ remained pale-brown even after 2–3 h of the reaction, but the yield of the MnO_x solids (estimated by weighing the dried product) under these conditions was no lower than with smaller ratios or with $Ca^{2+}_{(aq)}$ ions being present, that is, for dispersions in which the brown colour was achieved rapidly. In other words, following the reaction kinetics by using spectrophotometry was not possible, as the dispersions of materials produced under different conditions appear to differ in their light-absorption capacity. Generally, 2–3 h of mineralisation was sufficient to obtain MnO_x with a 50–70% yield, calculated with the assumption that the minerals have the stoichiometry of anhydrous MnO_2. However, given the milligram-scale of the synthesis procedures and the ambiguities in the actual composition of the produced materials, the determination of yield by weighing the produced MnO_x is uncertain. However, this uncertainty is not particularly important here because the kinetics of the processes are not being compared quantitatively.

Intriguing differences in the biogenic MnO_x produced under different conditions were revealed by microscopic analysis, the results of which are presented in Figures 2–4. When the MnxEFG-catalysed oxidation of $Mn^{2+}_{(aq)}$ occurs in $Ca^{2+}_{(aq)}$- and $Fe^{2+}_{(aq)}$-free solutions, changing the $c_{Mn(II)}$:c_{MnxEFG} ratio allows reproducible control over the morphology of the resulting manganese oxide solids, as best seen in the SEM images (Figure 2). At the lowest substrate concentration employed ($c_{Mn(II)}$:$c_{MnxEFG}=1.0\times10^4$), minerals formed as coarse agglomerates, probably composed of comparatively large MnO_x sheets (Figure 2a). Increasing the $c_{Mn(II)}$:c_{MnxEFG} ratio to 2.5×10^4 led to formation of non-agglomerated but strongly entangled manganese oxide sheets of at least several hundred nm in length (Figure 2b) and thickness of only few nanometres, as is evident in the side-view TEM images (Figure 4a). TEM also indicates that these MnO_x aggregates exhibit a layered structure of organised sheets. Further increases in the $Mn^{2+}{}_{(aq)}$ concentration causes significant changes in the morphology, namely, formation of rods in addition to sheets at $c_{Mn(II)}$:$c_{MnxEFG}=5.0\times10^4$ (Figure 2c) with the rod shape becoming dominant at $c_{Mn(II)}$:$c_{MnxEFG}=10\times10^4$ (Figure 2d). Similarly to the MnO_x sheets, the rods extend up to several hundred nanometres in length and are thin, with the diameter typically below 20 nm. Higher magnification TEM imaging (Figure 4b) reveals that MnO_x sheets are polycrystals comprised of randomly aligned nanometer-sized crystallites, while the rods appear to be built of crystallite planes with a strong preference for axial orientation.

It was generally hard to obtain highly informative selected-area electron-diffraction (SAED) data with well-defined diffraction maxima, which was not unexpected for these materials. One of the best results is exemplified in top right Figure 4a, in which the SAED pattern contains a set of reflections corresponding to a pseudo-hexagonal symmetry with interplane distances of 0.24 and 0.14 nm. In principle, these observations

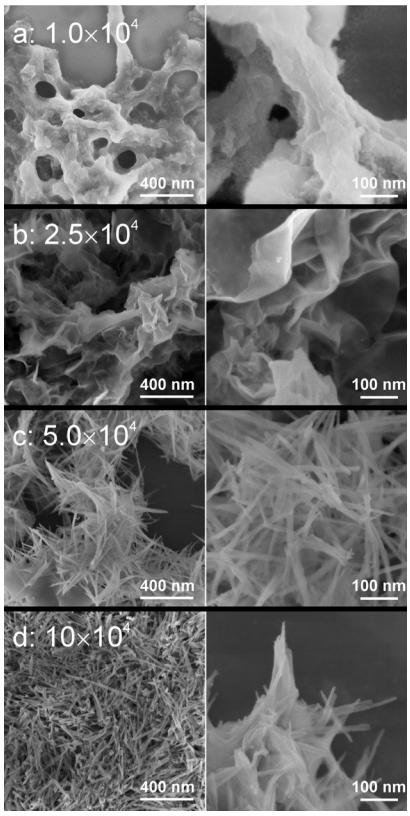

Figure 2. SEM images of the biogenic MnO_x minerals produced using different $c_{Mn(II)}$:c_{MnxEFG} ratios in 20 nM MnxEFG solutions (10 mM HEPES + 50 mM NaCl, pH 7.8).

are consistent with the MnO_2 structure (PDF #00-030-0820), although a similar diffraction pattern would be expected for birnessites with only slightly larger *d*-spacings.[14] The structures are so similar that it would be difficult to confidently distinguish them using these methods. More commonly observed were regions with somewhat amorphous or very finely polycrystalline ring ("powder") SAED patterns (bottom right Figure 4a), with two diffraction rings approximately corresponding to the interplane distances of about 0.14 and 0.24 nm irrespective of the $c_{Mn(II)}$:c_{MnxEFG} ratio.

The presence of $Ca^{2+}_{(aq)}$ during the MnxEFG-catalysed mineralisation did not induce noteworthy changes in the morphology of the produced solids at lower $c_{Mn(II)}$:c_{MnxEFG} (Figure 3a), but had a significant effect for $c_{Mn(II)}$:$c_{MnxEFG}=10\times10^4$ (Figure 3b, c). At this higher $Mn^{2+}_{(aq)}$ concentration (2 mM), and in the presence of a significant amount of $Ca^{2+}_{(aq)}$ (200 mM), the rod-type morphology was entirely eliminated and fine MnO_x sheets were exclusively observed, similar to those found with $c_{Mn(II)}$:$c_{MnxEFG}=2.5\times10^4$ (Figure 3b). This result is consistent with the qualitative observations of the colour of the produced MnO_x suspension in the presence and absence of $Ca^{2+}_{(aq)}$. In the presence of calcium ions, the solids quickly turned deep brown but, in contrast, in the absence of dissolved calcium, the solids were dark yellow (Figure 1). Reducing the concentration of calcium to 2 mM results in the formation of an interesting mixture of segregated rods and sheets (Figure 3c), which contrasts to the

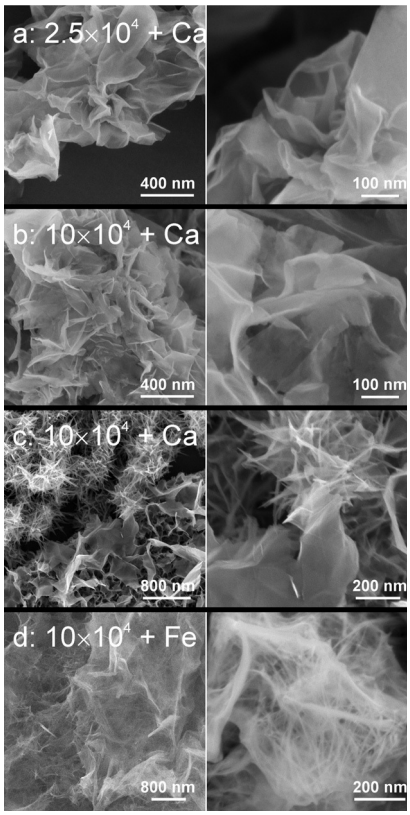

Figure 3. SEM images of the biogenic MnO_x minerals produced in the presence of $Ca^{2+}_{(aq)}$ or $Fe^{2+}_{(aq)}$ using different $c_{Mn(II)}$:c_{MnxEFG} ratios in 20 nM MnxEFG solutions (10 mM HEPES + 50 mM NaCl, pH 7.8). The concentration of $Ca^{2+}_{(aq)}$ was a), b) 200 and c) 2 mM; concentration of $Fe^{2+}_{(aq)}$ was d) 0.2 mM.

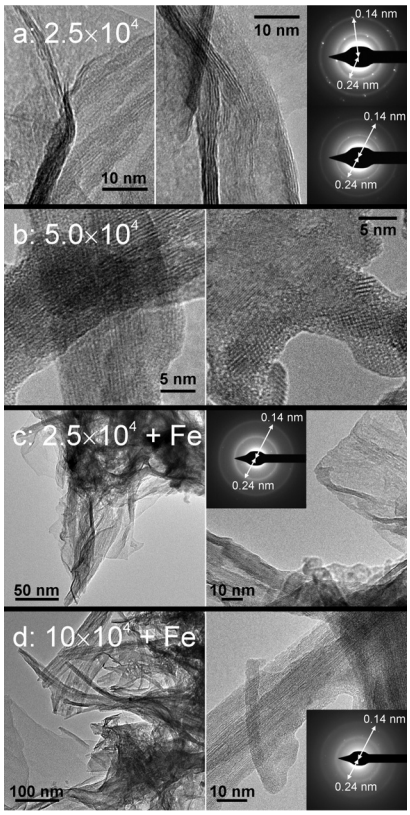

Figure 4. TEM images and SAED patterns for the biogenic MnO_x minerals produced in the absence a), b), and in the presence c), d) of $Fe^{2+}_{(aq)}$ using different $c_{Mn(II)}$:c_{MnxEFG} ratios (shown in Figure) in 20 nM MnxEFG solutions (10 mM HEPES + 50 mM NaCl, pH 7.8). The concentration of $Fe^{2+}_{(aq)}$ was c) 0.05 and d) 0.2 mM.

material produced in the $Ca^{2+}_{(aq)}$-free solutions with $c_{Mn(II)}$:$c_{MnxEFG} = 5.0\times10^4$ for which the two morphologies form and are homogeneously intermixed (Figure 2c). Probing local chemical composition of the MnO_x biogenic minerals formed in the presence of high concentrations of $Ca^{2+}_{(aq)}$ by using energy dispersive X-ray (EDX) analysis under SEM and TEM conditions revealed a homogeneous incorporation of calcium into the material, at the level of about 15–20 at.% with respect to manganese.

Limited solubility of $Fe^{2+}_{(aq)}$ under pH conditions employed here required us to study mineralisation with sub-millimolar concentrations of this cation, the ratio of which was kept constant relative to $c_{Mn(II)}$ ($c_{Fe(II)} = 0.1\ c_{Mn(II)}$) as the $c_{Mn(II)}$:c_{MnxEFG} ratio was varied. Weak magnetic properties exhibited by MnO_x produced under these conditions prevented the use of high-resolution SEM for morphology studies (a typical lower-resolution micrograph is shown in Figure 3d), and major conclusions were derived from the examination of the TEM data. Similarly to experiments with $Ca^{2+}_{(aq)}$, no evident influence of the presence of dissolved Fe^{2+} on the morphology of MnO_x was found at lower $Mn^{2+}_{(aq)}$ concentration (0.5 mM; $c_{Mn(II)}$:$c_{MnxEFG} = 2.5\times10^4$) (Figure 4c), but significant changes were observed when $c_{Mn(II)} = 2$ mM (Figure 4d). The material generated by the MnxEFG enzyme at $c_{Mn(II)}$:$c_{MnxEFG} = 10\times10^4$ with $Fe^{2+}_{(aq)}$ in solution was dominated by a sheet morphology that was homogeneously mixed with thin rods (Figure 4d). The amount of iron incorporated into biogenic MnO_x was independent of the $c_{Mn(II)}$:c_{MnxEFG} ratio and was approximately 7–9 at.% with respect to manganese, as determined by local EDX analysis under SEM and TEM conditions. No indication of the segregation of iron (hydr)oxide phases was found, that is, those are most probably co-precipitated homogeneously with MnO_x. The SAED patterns remained essentially unchanged when $Ca^{2+}_{(aq)}$ and $Fe^{2+}_{(aq)}$ were added to the mineralisation solutions and were again dominated by two ring-diffraction signals corresponding to the interplanar spacings of about 0.14 and 0.24 nm. The only difference observed was in the intensities of the diffraction signals, which were always notably weaker for materials obtained at $c_{Mn(II)}$:$c_{MnxEFG} = 10\times10^4$ and with $Fe^{2+}_{(aq)}$ present than for those with no iron.

Electronic state of Mn and structure

In principle, X-ray photoelectron spectroscopy (XPS) can be used to determine the oxidation state and electronic properties of metals. However, manganese presents a serious challenge for both qualitative and, in particular, quantitative analysis. It has six stable oxidation states (0, II, III, IV, VI and VII), three oxidation states with significant multiplet splitting (II, III, IV), one state with less defined splitting or broadening (VI) and

overlapping binding energy ranges for these multiplet splitting structures. The evaluation and interpretation of our data is based mainly on a recent publication by Biesinger et al.[15] who studied a range of different manganese reference materials in order to develop a reliable and consistent approach to the analysis of the manganese compounds in general. Herein, we restrict the discussion to a qualitative evaluation of the XPS data, mainly focusing on the Mn 2p spectra.

Representative model Mn 2p spectra of each oxidation state were generated using the tabulated parameters.[15] These are compared to the corresponding spectra of different biogenic manganese oxides in Figure 5a. We conclude that the dominant oxidation state present in the examined biogenic MnO_x minerals is Mn^{IV}, in keeping with previous reports,[8a,11d] and there are also minor contributions from Mn^{II} and Mn^{III}. Neither higher oxidation states (VI or VII) nor manganese metal were detected, as expected. From this perspective, the materials can be regarded as MnO_2 with small proportions of species such as MnO, Mn_2O_3 and MnO(OH). However, it is also noted that the XP spectra for biogenic MnO_x were very similar to that recorded for manganese oxides obtained by oxidative electrodeposition (Figure S1 in the Supporting Information), that is, under conditions that favour the formation of the birnessite phase.[16]

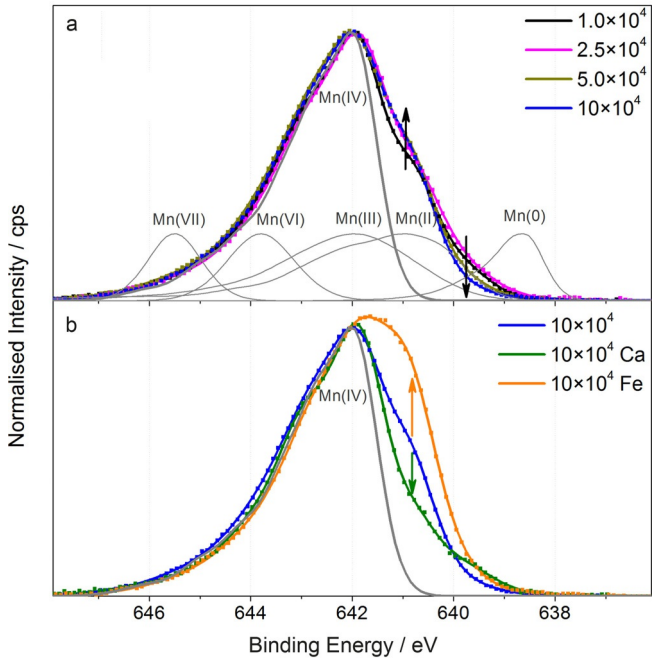

Figure 5. Core-level Mn 2p spectra of the biogenic MnO_x minerals showing the effect of a) increasing the $c_{Mn(II)}$:c_{MnxEFG} ratio (1.0×10^4-*black*, 2.5×10^4-*magenta*, 5.0×10^4-*tan*, 10×10^4-*blue*), and b) the presence of 200 mM Ca^{2+} (*green*) or 0.2 mM Fe^{2+} (*orange*) during mineralisation at $c_{Mn(II)}$:$c_{MnxEFG}=10\times10^4$. Other mineralisation conditions as in Figure 2. *Grey* curves show representative model spectra of the six different Mn oxidation states[15] (see labels in figure).

Variations in the $c_{Mn(II)}$:c_{MnxEFG} ratio within the examined range induced minor but clearly identifiable changes in the electronic state of Mn in the biogenic minerals. The apparent degree of oxidation of manganese increases slightly with increasing the $c_{Mn(II)}$:c_{MnxEFG} ratio from 1.0×10^4 to 10×10^4, as concluded on the basis of the shift of spectral intensity from lower (639–640 eV) to higher binding energy (641 eV). Correlation of these changes with the reference manganese spectra in Figure 5a suggests that the contribution from the Mn^{II} component increases and the Mn^{III} portion decreases in MnO_x when lower initial concentrations of $Mn^{2+}_{(aq)}$ in the mineralisation mixture are used, which might seem counterintuitive at first glance. However, decreased contribution from Mn^{III} at lower $c_{Mn(II)}$:c_{MnxEFG} most probably indicates deeper oxidation of manganese to the Mn^{IV} state, which is expected when more catalyst (MnxEFG) per mol of the substrate ($Mn^{2+}_{(aq)}$) is available. Minor enhancements in the amount of Mn^{II} detected by the surface-sensitive XPS technique are interpreted in terms of differences in the amount of the unreacted substrate adsorbed on the material surface, or trapped in the near-surface layers, during sedimentation.

Introduction of $Ca^{2+}_{(aq)}$ or $Fe^{2+}_{(aq)}$ into the reaction mixture induced more significant changes in the MnO_x electronic state, as compared to the effect of the variations in the substrate-to-MnxEFG ratio. Biogenic mineralisation in the presence of high concentrations of $Ca^{2+}_{(aq)}$ promoted formation of more deeply oxidised MnO_x with XP spectra resembling closely those of Mn^{IV}, having significantly suppressed Mn^{III} contributions, as compared to the calcium-free conditions (Figure 5b). Interestingly, this result contrasts to the previous XAS study on MnO_x produced by marine *Bacillus* spores containing the same MnxG enzyme,[11e] in which an opposite effect of $Ca^{2+}_{(aq)}$ on the average manganese oxidation state was found. Most probably, this is due to the very different mineralisation conditions (including solute concentrations and the strain of spores) used by Webb et al., leading to the formation of different MnO_x phase(s).[11e] The presence of $Fe^{2+}_{(aq)}$ under our conditions allows formation of notably more reduced manganese minerals, with increased relative fractions of Mn^{II} and Mn^{III} (Figure 5b). On a qualitative level, this finding is consistent with the suppressed rates of mineralisation when small amounts of $FeCl_2$ were added (vide supra). The effects of $Ca^{2+}_{(aq)}$ and $Fe^{2+}_{(aq)}$ on the electronic state of manganese described above were found for lower (2.5×10^4) and higher (10×10^4) $c_{Mn(II)}$:c_{MnxEFG} ratios. Consistent with the EDX analyses, incorporation of both calcium (about 10–20 at.%) and iron (about 5 at.%) into the MnO_x minerals was confirmed by the XPS data, but establishing the electronic state of iron was not possible due to the very low signal-to-noise ratio and insufficient resolution of the core level Fe 2p spectra.

The XAS data sets for the examined biogenic MnO_x minerals are consistent with the birnessite phase predominating for all $c_{Mn(II)}$:c_{MnxEFG} ratios tested (Figure 6a–c and Figure S2 in the Supporting Information). There was also Mn^{II} present at the level of about 15 at.%, as concluded from analysis of the X-ray absorption near edge structure (XANES) data (Figure S2a), in keeping with the XPS results. This observation suggests that unreacted Mn^{II} species are not only adsorbed on the surface of the materials, but are also trapped in the bulk structure during sedimentation. Data shown in Figure 6c demonstrate the

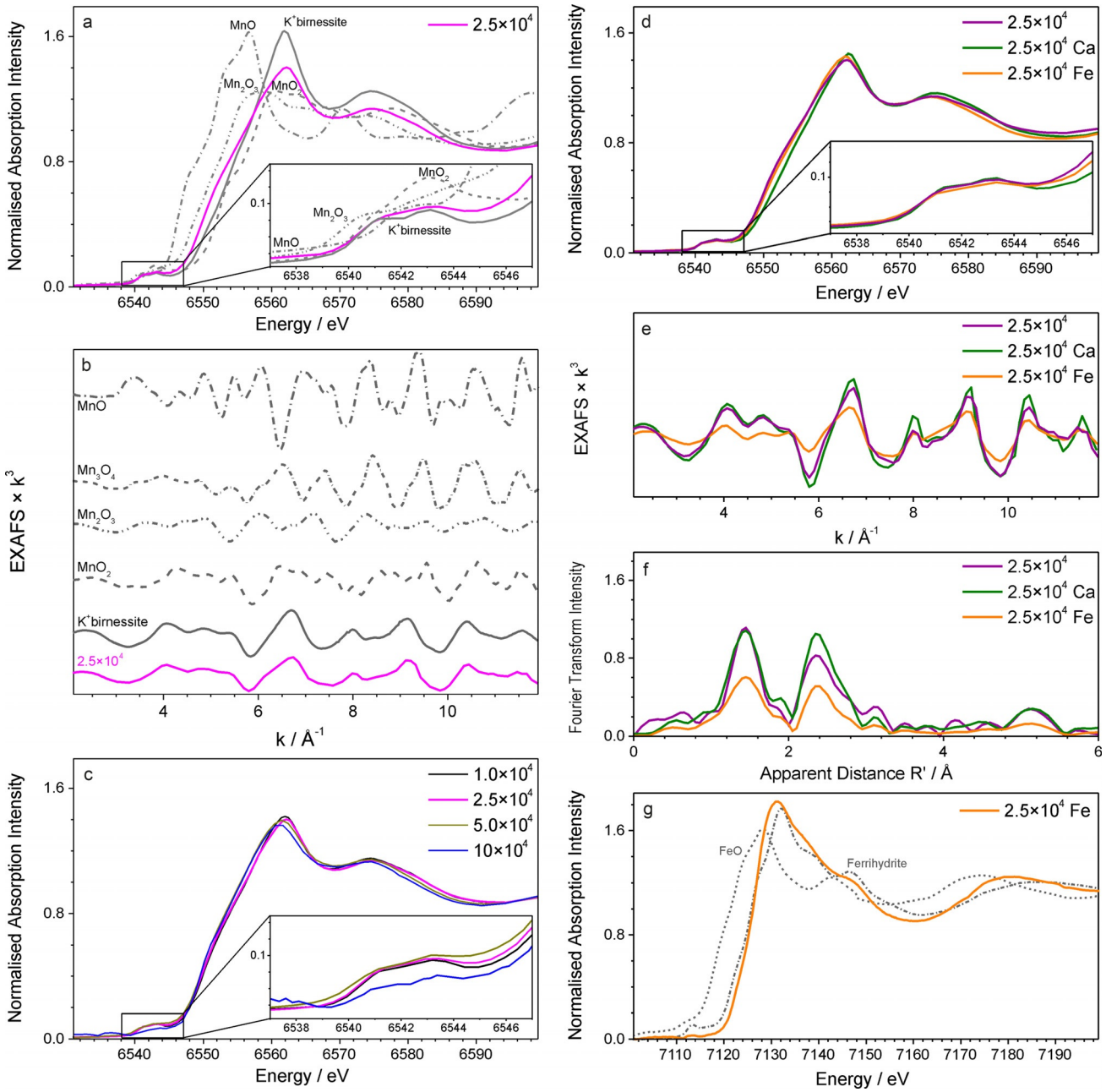

Figure 6. a)–f) Mn K-edge and g) Fe K-edge XAS data taken on the biogenic MnO_x minerals synthesised at different $c_{Mn(II)}$:c_{MnxEFG} ratios (1.0×10^4-*black*, 2.5×10^4-*magenta* (a–c) or *purple* (d–f), 5.0×10^4-*tan*, 10×10^4-*blue*), and in the presence of 200 mM Ca^{2+} (*green*) or 0.05 mM Fe^{2+} (*orange*) during mineralisation at $c_{Mn(II)}$:$c_{MnxEFG}=2.5\times10^4$. Panels a), c), d) and g) show XANES spectra with pre-edge in the insets (a, c, d); panels b) and e) show EXAFS; panel f) shows Fourier transform of the EXAFS. Panels a), b) and g) show data for the standard reference compounds as grey traces.

effect that changing the manganese-to-protein ratio has on the average oxidation state of the metal. It is clear from the XANES data that the degree of oxidation of manganese in the minerals produced by the MnxEFG protein complex increases slightly as the $c_{Mn(II)}$:c_{MnxEFG} ratio decreased from 10×10^4 to 1.0×10^4. Moreover, the structure becomes more ordered, as evident from the increase in the Fourier-transformed XAS intensity when lower initial concentrations of $Mn^{2+}_{(aq)}$ are used, although the changes are not striking (Figure S2b), which is in sharp contrast to the dramatically different morphologies (Figure 2) created by the different solutions. The detected structural changes appear to be consistent with small amounts of trapped residual Mn^{2+}, which becomes larger when the $c_{Mn(II)}$:c_{MnxEFG} ratio is increased.

Significantly more pronounced differences in the MnO_x structure, and in the manganese oxidation state, were found when mineralisation was undertaken in the MnxEFG solutions containing $Ca^{2+}_{(aq)}$ or $Fe^{2+}_{(aq)}$, as can be seen in Figures 6d–f. Mineralisation in the presence of $Ca^{2+}_{(aq)}$ promotes a more complete oxidation to birnessite (Figure 6d), and formation of more ordered MnO_x minerals than those produced without calcium (Figure 6e,f). The effect was found for both $c_{Mn(II)}$:$c_{MnxEFG}=$

2.5×10^4 and 10×10^4 and was more pronounced for the lower initial concentration of $Mn^{2+}_{(aq)}$. The presence of $Ca^{2+}_{(aq)}$ in substantial concentrations likely reduces the Mn^{II} content of the final material, resulting in a visibly stronger EXAFS associated with a less disordered structure. The opposite effect was induced by adding small amounts of $Fe^{2+}_{(aq)}$ to the mineralisation solutions, that is, the formation of slightly less oxidised but significantly more disordered MnO_x minerals was promoted (Figure 6d–f). Again, this result was reproduced for both higher and lower $Mn^{2+}_{(aq)}$ concentrations, though the structural changes were more pronounced for the higher $c_{Mn(II)}$:c_{MnxEFG} ratio in this case. Comparisons of the Fe K-edge XAS data obtained for the biogenic Fe:MnO_x materials with the standard references suggests that iron oxide solids formed under the employed mineralisation conditions have features in common with ferrihydrite (Figure 6g), although extended structural analysis was not possible because of the very low concentrations of FeO_x in the minerals. No unambiguous confirmation of incorporation of either $Fe^{II/III}$ or Ca^{II} into the MnO_x crystal structure could be derived from the available XAS data.

Implications of structural differences to chemical properties

The relation between the chemical reactivity of materials and their structure is central to the design of efficient metal oxide and other catalysts.[17] The variations in morphology and structure described above for the biogenic MnO_x minerals produced by the MnxEFG protein complex suggest that these materials should also differ in terms of their capacity to undergo chemical transformations and, conceivably, in their catalytic properties.

Some indication of the differences in reactivity of the examined MnO_x solids is obtained when comparing the XPS results for the freshly prepared materials to the films that were subjected to mild heating under ambient conditions at 90 °C for 30 min. Such treatment resulted in partial reduction of the surface manganese species, namely, an increase in the $Mn^{II/III}$ contribution (Figure 7a). Reduction of the MnO_x surface by heating on air might be caused by the oxidation of adventitious carbon that was derived from volatile species, and/or from adsorbed organic compounds (possibly, including MnxEFG) by oxidised manganese. This effect was most pronounced for the materials that were initially more oxidised, that is, those obtained with the lowest $c_{Mn(II)}$:c_{MnxEFG} ratios, while the biogenic minerals that were initially more reduced demonstrated smaller changes in the manganese redox state (Figure 7b). Moreover, the samples with the most reduced surfaces, that is, those obtained in the presence of $Fe^{2+}_{(aq)}$, suffered slight oxidation rather than reduction when heated on air.

Further, the capacity of MnO_x to photo-oxidise a model organic compound, namely D-glucose, was assessed by irradiating the dispersions of minerals in 10 mM aqueous solutions of the monosaccharide. In these experiments, all minerals were obtained at $c_{Mn(II)}$:$c_{MnxEFG}=10\times10^4$ and the effects of $Ca^{2+}_{(aq)}$ and $Fe^{2+}_{(aq)}$ were examined (Figure 7c). Comparisons of the manganese K-edge positions and shapes in the XANES spectra for the untreated and photo-reduced materials confirm the ability of biogenic MnO_x to oxidise organics, which is, of course, a

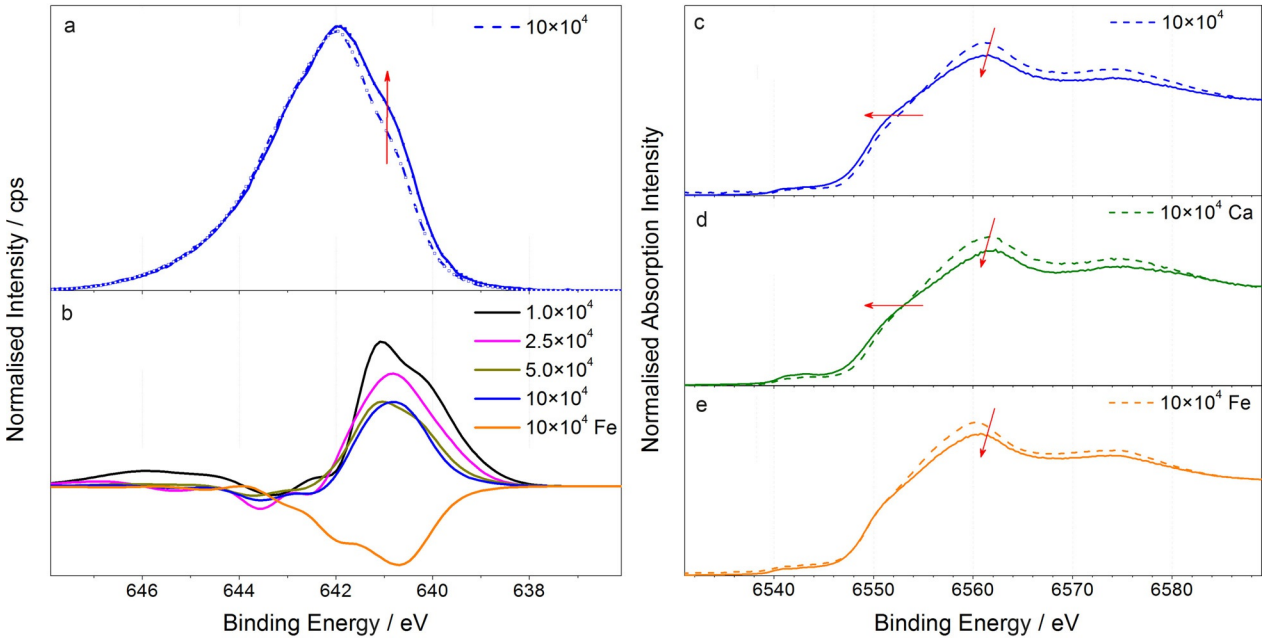

Figure 7. Changes in the a), b) XPS and c)–e) XANES data for biogenic MnO_x induced by a), b) heat-treatment of solid films on air (90 °C; 30 min) and c)–e) irradiation of the dispersions of the minerals in aqueous 10 mM D-glucose solutions (see the experimental section for details). Panel b) shows difference XP spectra for both heated and untreated minerals; given the well-known ambiguities in presenting the XPS data in this format, original background-corrected spectra are additionally shown in Figure S1 (Supporting Information). In panels a) and c)–e), dashed lines and solid curves show the spectra before, and after, treatment, respectively, and arrows indicate the changes that were induced by treatment. Minerals were obtained with $c_{Mn(II)}$:$c_{MnxEFG}=1.0\times10^4$ (*black*), 2.5×10^4 (*magenta*), 5.0×10^4 (*tan*), and 10×10^4 (*blue*), and in the presence of $Ca^{2+}_{(aq)}$ (*green*) or $Fe^{2+}_{(aq)}$ (*orange*) at $c_{Mn(II)}$:$c_{MnxEFG}=10\times10^4$. Other MnO_x-mineralisation conditions are defined in the caption of Figure 2 and in the associated text.

well-known and important natural function of these minerals. Inspection of the data in Figure 7c suggests that the photochemical process is not fast and may be hampered by the slow removal of the reduced $Mn^{III/II}$ species from the minerals surface. The resulting comparatively small changes in the XANES data do not allow a confident conclusion to be drawn from the differences in the photo-oxidation reactivity of MnO_x, Ca:MnO_x and Fe:MnO_x.

Finally, selected MnO_x minerals were tested for their electrocatalytic activity towards the oxidation of water. The structure of the metal oxide catalysts is well-established to be a critical parameter determining their performance.[18] The water electrooxidation activity of MnO_x produced by the MnxEFG protein complex was evaluated by depositing the materials onto F:SnO_2-coated glass slides that were used as working electrodes in order to record cyclic voltammograms and chronoamperograms up to very positive potentials in aqueous 0.5 M NaOH.

The electrocatalytic activities were not high, as exemplified for the unmodified and calcium- or iron-modified MnO_x solids obtained with $c_{Mn(II)}$:$c_{MnxEFG} = 10 \times 10^4$ in Figure 8. As a matter of fact, the electrocatalytic performance of the F:SnO_2 electrode sometimes deteriorated rather than improved upon functionalisation with some of the biogenic minerals. The electrocatalytic activity of unmodified F:SnO_2 is mainly due to the contribution of minor metal oxide admixtures.[19] All of the examined MnO_x materials exhibited very low photo-current densities for water oxidation under 1 sun simulated AM1.5G irradiation within the potential range relevant to Figure 8, which were typically below 5 $\mu A\,cm^{-2}$ (data not shown).

These findings are unexpected given the structural similarities between the biogenic materials and birnessite (vide supra), which is recognised as a catalytically active phase of manganese oxide solids during water electrooxidation.[16] Heat-treatment of the electrodes to increase the Mn^{III} contribution (Figure 7 and Figure S1 in the Supporting Information), which is critical for efficient catalysts of water oxidation,[18b] did not improve the activity of the biogenic MnO_x. At the same time, continuous polarisation at very positive potentials, namely, >1.9 V vs. RHE, slightly enhanced the electrocatalytic capacity of the Ca:MnO_x and MnO_x materials (Figure 8). Although no new elements on the electrode surface could be detected by XPS after these experiments, we cannot completely rule out the possibility that the electrodes became contaminated with adventitious iron, or other metals, from the electrolyte solutions. Such contamination during the long-term chronoamperometric experiments might account for the observed increase of the water-oxidation current density. However, it is noted that blank F:SnO_2 and Fe:MnO_x-modified electrodes did not demonstrate a similar effect under the same conditions, and that significantly less positive potentials than 1.9 V vs. RHE are needed to initiate electrodeposition of FeO_x. Arguably, partial dissolution–redeposition of manganese oxide solids at very positive potentials and restructuring of the MnO_x surface might be a plausible explanation for the minor improvements in the catalytic activity that we detect.

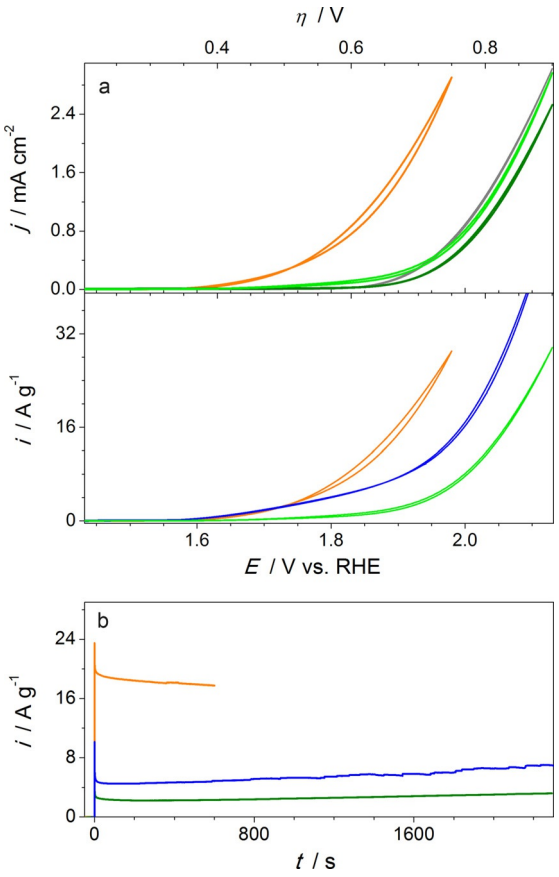

Figure 8. a) Cyclic voltammograms (scan rate 0.010 $V\,s^{-1}$) and b) chronoamperograms at 1.93 V vs. RHE (water oxidation overvoltage, $\eta = 0.70$ V) measured for the biogenic MnO_x synthesised at $c_{Mn(2+)}$:$c_{MnxEFG} = 10 \times 10^4$ in the absence of $Fe^{2+}_{(aq)}$ and $Ca^{2+}_{(aq)}$ (blue; voltammogram was obtained after measuring chronoamperogram shown in b), and in the presence of 0.2 mM $Fe^{2+}_{(aq)}$ (*orange*) or 200 mM $Ca^{2+}_{(aq)}$ (*green* and *light green* data in a) were obtained before and after recording chronoamperogram shown as *green* in b), respectively). Top and bottom plots in a) show data normalised to the geometric surface area and mass of MnO_x, respectively. *Grey* curve in a) shows data for the MnO_x-free F:SnO_2 electrode. Electrolyte: 0.5 M $NaOH_{(aq)}$.

Most importantly, data in Figure 8 suggest that the more structurally ordered Ca-modified MnO_x are less catalytically active than the more disordered Ca-free minerals obtained at $c_{Mn(II)}$:$c_{MnxEFG} = 10 \times 10^4$. Furthermore, modification of MnO_x with iron oxide solids, as achieved by mineralisation in the presence of $Fe^{2+}_{(aq)}$, significantly enhances the electrocatalytic performance. However, discrimination between the effects of significant disorder in the MnO_x structure, higher contribution from Mn^{III}, or the presence of FeO_x on the catalytic activity, is exceptionally difficult.

Overall, the reactivity of the MnO_x solids examined herein was small, and is probably typical for the biogenic minerals, even though they were produced under conditions not characteristic of the ocean environment. The differences in the extent of structural disorder was insufficient to cause large changes in the capacity of biogenic MnO_x to (photo)oxidise organic compounds, at least under these conditions, but some differences in the catalytic activity towards water electrooxidation in alkaline solutions were observed.

Conclusion

The MnxEFG protein complex enables mineralisation of birnessite-like solids with strikingly different morphologies and with different levels of structural disorder. Importantly, these properties can be easily controlled by changing the composition of the mineralisation solutions, indicating a strategy to tune the morphology of MnO_x on the nanometre-size scale and to direct the formation of very thin rods, or thin sheets, by simply varying the $Mn^{2+}_{(aq)}$-to-protein ratio, or by introducing other metal cations. Interestingly, the MnxEFG-catalysed mineralisation in the presence of $Ca^{2+}_{(aq)}$ or $Fe^{2+}_{(aq)}$ allows these elements to be included into the resulting MnO_x solids, although it is not clear if the cations are incorporated into the MnO_x crystal structure.

The (photo)oxidation capacity and catalytic activity for water (photo)electrooxidation of the MnO_x minerals were comparatively low and differed slightly depending on the level of structural disorder and with the presence of iron. This relative chemical inertness of the solids, coupled to the remarkable tunability of the morphology of biogenic MnO_x, makes these materials attractive as conductive supports or high-surface-area electrodes for applications where stability is critical. Given the impressive tolerance of the MnxEFG protein complex to widely differing experimental conditions, we anticipate that it will be possible to tune the properties of biogenic MnO_x broadly for various applications.

Experimental Section

Materials: The MnxEFG protein complex (*mnx*E_3F_3G, ca. 211 kDa) was obtained as reported elsewhere.[8a] Reagent- or analytical-grade chemicals were used as received from commercial suppliers. High purity water (18 MΩ cm; Sartorius Arium 611) was used for all experimental procedures. Before use, all glassware was cleaned by soaking in a freshly prepared H_2SO_4 (98 wt.%):H_2O_2 (30 vol.%) (1:1 vol.) mixture for at least 12 h and then by rinsing with copious amounts of water.

Mineralisation experiments: Biogenic MnO_x minerals were obtained by aerobic oxidation of solutions containing different amounts of $Mn^{2+}_{(aq)}$. The substrate was added as an aliquot of 100 mM $MnCl_{2(aq)}$ to a 20 nM MnxEFG protein complex solution in water containing 10 mM 4-(2-hydroxyethyl)piperazine-1-ethanesulfonic acid (HEPES) and 50 mM NaCl (pH 7.8). In some experiments, $CaCl_2$ or $FeCl_2$ was added to the reaction mixture along with the aqueous $MnCl_2$ aliquot. Mineralisation typically occurred for approximately 2–3 h, except for the experiments undertaken in the presence of $Fe^{2+}_{(aq)}$ with the $c_{Mn(2+)}$:$c_{MnxEFGaq)}$ ratio of 10×10^4, in which cases the reaction was allowed to occur for 20 h. Stirring the solutions induced sedimentation of MnO_x in the form of crude aggregated flakes, so the reaction mixtures were kept quiescent to allow for homogeneous mineralisation of the materials. Solids were separated from the protein solution by centrifugation followed by washing and sonication in water for 5–10 min. The washing procedure was repeated at least four times. Each repetition employed a fresh portion of water after centrifugation and decantation to eliminate the previous supernatant solution. The resulting slurry was separated into parts, one of which was dried under vacuum to obtain dry mineral and another was stored as a dispersion of MnO_x solids in water. The latter was saved for preparing samples for microscopic analysis, as the biogenic minerals produced under most conditions could not be redispersed in water after being fully dried.

Scanning electron microscopy (SEM): SEM with local energy dispersive X-ray (EDX) analysis of all materials, except those containing iron, was undertaken using a FEI Magellan 400 FEG SEM. MnO_x synthesised in the presence of $Fe^{2+}_{(aq)}$ exhibited weak magnetic properties, which precluded their characterisation in the "immersion mode" on a Magellan SEM, which can be easily contaminated by magnetic materials. Thus, Fe-containing solids were studied using a JEOL7001F FEG SEM instrument in a field-free mode, which is less susceptible to contamination by this sort of materials. For analysis, the MnO_x minerals were deposited as thin layers on a silicon wafer that was glued to a SEM specimen stub and electrically connected by a copper tape.

Transmission electron micrographs (TEM): TEM with local EDX analysis and selected-area electron diffraction (SAED) patterns for minerals deposited on a holey carbon grid were obtained using a Tecnai G2 T20 TWIN instrument with a point resolution of 0.27 nm and equipped with a Bruker Quantax 200 X-Ray analysis system.

X-ray photoelectron spectroscopy (XPS): XPS was performed using either an AXIS Ultra DLD or an AXIS Nova spectrometer (Kratos Analytical Inc., Manchester, UK) with a monochromated aluminum Kα source at a power of 180 W (15 kV×12 mA), a hemispherical analyser operating in fixed-analyser transmission mode and with the standard aperture (analysis area: 0.3 mm × 0.7 mm). The total pressure in the main vacuum chamber during analysis was typically between 10^{-9} and 10^{-8} mbar. Survey spectra were acquired at a pass energy of 160 eV. To obtain more detailed information about chemical structure, oxidation states etc., high resolution spectra were recorded from individual peaks at 40 eV pass energy (yielding a typical peak width for polymers of <1.0 eV).

Samples for analysis were prepared by drop-casting an aqueous suspension of the material on a glass covered with fluorine-doped tin oxide (F:SnO_2) or high-purity silicon wafer and drying under ambient conditions; in some cases, the samples were additionally heated at 90 °C for 30 min. Each specimen was analysed at an emission angle of 0° from the surface normal. Assuming typical values for the electron attenuation length of relevant photoelectrons, the XPS analysis depth (from which 95% of the detected signal originates) ranged between 5 and 10 nm for a flat surface. Data processing was performed using CasaXPS processing software version 2.3.15 (Casa Software Ltd., Teignmouth, UK). All elements present were identified from survey spectra. The atomic concentrations of the detected elements were calculated using integral peak intensities and the sensitivity factors supplied by the manufacturer. Binding energies were referenced to the C 1s peak at 284.8 eV (adventitious hydrocarbon). The accuracy associated with quantitative XPS is about 10–15%. Precision (i.e., reproducibility) depends on the signal-to-noise ratio but is usually much better than 5%. This last statistic should be remembered when similar samples are compared.

X-ray absorption spectroscopy (XAS): Manganese and iron K-edge XA spectra were recorded on the multipole wiggler XAS beam-line 12 ID at the Australian Synchrotron in operational mode 1. The beam energy was 3.0 GeV and the maximum beam current was 200 mA. Data on the oxide powders were collected in transmission mode in helium-filled ionisation chambers. Samples for the transmission X-ray experiments were prepared by grinding the sample together with boron nitride and loading into a 1 mm thin aluminium spacer and sealed with 63.5 μm Kapton tape.[20] XAS data were analysed using a combination of PySpline[21] and

Microsoft Excel[22] for background subtractions, and Artemis[23] for the extended X-ray absorption fine structure (EXAFS) fitting. For EXAFS data, an E0 value of 6555.0 eV was used and data were calibrated against the first inflection point of a manganese foil 6539.0 eV.

Photoreduced samples of MnO_x were obtained by irradiating the dispersions of the materials (0.2 mL; 1 mg mL^{-1}) in aqueous 10 mM D-glucose (pH 5.5) using a 6300 lm/1000 W white light-emitting diode (LED) array installed *ca* 15 cm away from the sample for 6 h. The dispersions were extensively sonicated prior to experiments and placed inside quartz cuvettes, which were periodically shaken to maintain homogeneity. The irradiated dispersions were drop-casted onto a glass support and analysed in the fluorescence mode.

Electrochemical measurements: These were carried out in a standard three-electrode configuration with a Bio-Logic VSP workstation at ambient temperature (24±1 °C). The compartment for an auxiliary electrode (high-surface-area titanium wire) was separated from the working-electrode compartment with a P4 glass frit (10–16 μm pore size). The reference Ag|AgCl|KCl(sat.) electrode (CHI) was directly immersed in the working electrolyte solution and placed in close vicinity to the working electrode surface. Experimental potentials were converted to the reversible hydrogen electrode (RHE) scale using the Nernst equation. Glass covered with F:SnO_2 was laser engraved (Universal Laser Systems, Inc., VersaLaser VLS350) to define the circular electroactive area (ca. 0.19 cm^2) and used as a working-electrode substrate. The MnO_x solids were immobilised on F:SnO_2 by drop-casting about 30–40 μg cm^{-2} of the material from an extensively sonicated aqueous dispersion (ca. 1 mg mL^{-1}) under gentle Ar flow. In some cases, the electrodes were subsequently heated at 90 °C for 30 min on air. For photoelectrochemical experiments, a 150 W xenon arc lamp equipped with a horizontal light beam and an Oriel solar simulator with an AM 1.5G filter was used. The visible light intensity of 1 sun (AM 1.5G, 100 mW cm^{-2}) was calibrated using a reference solar cell that was obtained from CalLab, Frauenhofer ISE. The electrodeposited MnO_x films on F:SnO_2 were obtained using 1 mM $Mn(CH_3COO)_2$ solutions at a constant potential of 1.0 V vs. Ag|AgCl|KCl(sat.) for 90 s.

Acknowledgements

The authors thank the Monash Centre for Electron Microscopy for providing access to the facilities, the Australian Synchrotron for providing access to the XAS beam-line (project ID M9991) and beam-line scientists Dr. Bernt Johannessen, Dr. Peter Kappen and Dr. Chris Glover for support in experiments. Funding of this work by the Australian Research Council (CE140100012 to LS) and National Science Foundation (EAR1231322 to WHC and CHE1410688 to BMT) is gratefully appreciated.

Conflict of interest

The authors declare no conflict of interest.

Keywords: biogenic materials · manganese · MnxEFG protein complex · structural disorder · structure elucidation · tunable morphology

[1] E. D. Goldberg, *J. Geol.* **1954**, *62*, 249–265.
[2] M. M. Najafpour, M. Hołyńska, S. Salimi, *Coord. Chem. Rev.* **2015**, *285*, 65–75.
[3] a) B. M. Tebo, J. R. Bargar, B. G. Clement, G. J. Dick, K. J. Murray, D. Parker, R. Verity, S. M. Webb, *Annu. Rev. Earth Planet. Sci.* **2004**, *32*, 287–328; b) T. G. Spiro, J. R. Bargar, G. Sposito, B. M. Tebo, *Acc. Chem. Res.* **2010**, *43*, 2–9.
[4] a) Y. M. Nelson, L. W. Lion, M. L. Shuler, W. C. Ghiorse, *Environ. Sci. Technol.* **1996**, *30*, 2027–2035; b) B. Müller, L. Granina, T. Schaller, A. Ulrich, B. Wehrli, *Environ. Sci. Technol.* **2002**, *36*, 411–420; c) M. Berg, H. C. Tran, T. C. Nguyen, H. V. Pham, R. Schertenleib, W. Giger, *Environ. Sci. Technol.* **2001**, *35*, 2621–2626; d) L. E. Eary, D. Rai, *Environ. Sci. Technol.* **1987**, *21*, 1187–1193; e) M. C. Duff, D. B. Hunter, I. R. Triay, P. M. Bertsch, D. T. Reed, S. R. Sutton, G. Shea-McCarthy, J. Kitten, P. Eng, S. J. Chipera, D. T. Vaniman, *Environ. Sci. Technol.* **1999**, *33*, 2163–2169; f) D. W. Kennedy, J. K. Fredrickson, J. M. Zachara, Y. A. Gorby, A. Dohnalkova, M. Duff, *Abstr. Gen. Meet. Am. Soc. Microbiol.* **2000**, *100*, 494.
[5] W. G. Sunda, S. A. Huntsman, *Deep-Sea Res. Part A* **1988**, *35*, 1297–1317.
[6] a) B. G. Clement, G. W. Luther III, B. M. Tebo, *Geochim. Cosmochim. Acta* **2009**, *73*, 1878–1889; b) A. S. Madison, B. M. Tebo, A. Mucci, B. Sundby, G. W. Luther, *Science* **2013**, *341*, 875–878.
[7] a) C. R. Anderson, H. A. Johnson, N. Caputo, R. E. Davis, J. W. Torpey, B. M. Tebo, *Appl. Environ. Microbiol.* **2009**, *75*, 4130–4138; b) K. Nakama, M. Medina, A. Lien, J. Ruggieri, K. Collins, H. A. Johnson, *Appl. Environ. Microbiol.* **2014**, *80*, 6837–6842; c) P. F. Andeer, D. R. Learman, M. McIlvin, J. A. Dunn, C. M. Hansel, *Environ. Microbiol.* **2015**, *17*, 3925–3936.
[8] a) C. N. Butterfield, A. V. Soldatova, S.-W. Lee, T. G. Spiro, B. M. Tebo, *Proc. Natl. Acad. Sci. USA* **2013**, *110*, 11731–11735; b) L. Tao, T. A. Stich, C. N. Butterfield, C. A. Romano, T. G. Spiro, B. M. Tebo, W. H. Casey, R. D. Britt, *J. Am. Chem. Soc.* **2015**, *137*, 4054; c) Z. Zhang, Z. Zhang, H. Chen, J. Liu, C. Liu, H. Ni, C. Zhao, M. Ali, F. Liu, L. Li, *Sci. Rep.* **2015**, *5*, 10895; d) J. Su, L. Deng, L. Huang, S. Guo, F. Liu, J. He, *Water Res.* **2014**, *56*, 304–313; e) J. Su, P. Bao, T. Bai, L. Deng, H. Wu, F. Liu, J. He, *PLoS ONE* **2013**, *8*, e60573; f) K. Geszvain, L. Smesrud, B. M. Tebo, *Appl. Environ. Microbiol.* **2016**, *82*, 3774–3782.
[9] a) E. I. Solomon, U. M. Sundaram, T. E. Machonkin, *Chem. Rev.* **1996**, *96*, 2563–2606; b) E. I. Solomon, R. K. Szilagyi, S. DeBeer, G. L. Basumallick, *Chem. Rev.* **2004**, *104*, 419–458.
[10] a) S. M. Webb, G. J. Dick, J. R. Bargar, B. M. Tebo, *Proc. Natl. Acad. Sci. USA* **2005**, *102*, 5558–5563; b) K. Toyoda, B. M. Tebo, *Geochim. Cosmochim. Acta* **2013**, *101*, 1–11; c) A. Soldatova, C. Butterfield, O. Oyerinde, B. Tebo, T. Spiro, *JBIC J. Biol. Inorg. Chem.* **2012**, *17*, 1151–1158.
[11] a) K. W. Mandernack, J. Post, B. M. Tebo, *Geochim. Cosmochim. Acta* **1995**, *59*, 4393–4408; b) J. R. Bargar, B. M. Tebo, J. E. Villinski, *Geochim. Cosmochim. Acta* **2000**, *64*, 2775–2778; c) J. R. Bargar, B. M. Tebo, U. Bergmann, S. M. Webb, P. Glatzel, V. Q. Chiu, M. Villalobos, *Am. Mineral.* **2005**, *90*, 143–154; d) S. M. Webb, B. M. Tebo, J. R. Bargar, *Am. Mineral.* **2005**, *90*, 1342–1357; e) S. M. Webb, B. M. Tebo, J. R. Barger, *Geomicrobiol. J.* **2005**, *22*, 181–193.
[12] K. Toyoda, B. M. Tebo, *Geochim. Cosmochim. Acta* **2016**, *189*, 58–69.
[13] a) C. N. Butterfield, L. Tao, K. N. Chacón, T. G. Spiro, N. J. Blackburn, W. H. Casey, R. D. Britt, B. M. Tebo, *Biochim. Biophys. Acta Proteins Proteomics* **2015**, *1854*, 1853–1859; b) L. Tao, A. N. Simonov, C. A. Romano, C. N. Butterfield, M. Fekete, B. M. Tebo, A. M. Bond, L. Spiccia, L. L. Martin, W. H. Casey, *Chem. Eur. J.* **2017**, *23*, 1346–1352; c) L. Tao, A. N. Simonov, C. A. Romano, C. N. Butterfield, B. M. Tebo, A. M. Bond, L. Spiccia, L. L. Martin, W. H. Casey, *ChemElectroChem* **2017**, https://doi.org/10.1002/celc.201700563.
[14] V. A. Drits, E. Silvester, A. I. Gorshkov, A. Manceau, *Am. Mineral.* **1997**, *82*, 946–961.
[15] M. C. Biesinger, B. P. Payne, A. P. Grosvenor, L. W. M. Lau, A. R. Gerson, R. S. C. Smart, *Appl. Surf. Sci.* **2011**, *257*, 2717–2730.
[16] R. K. Hocking, R. Brimblecombe, L.-Y. Chang, A. Singh, M. H. Cheah, C. Glover, W. H. Casey, L. Spiccia, *Nat. Chem.* **2011**, *3*, 461–466.
[17] a) T. Zambelli, J. Wintterlin, J. Trost, G. Ertl, *Science* **1996**, *273*, 1688–1690; b) J. A. Switzer, H. M. Kothari, P. Poizot, S. Nakanishi, E. W. Bohannan, *Nature* **2003**, *425*, 490–493; c) O. V. Cherstiouk, A. N. Gavrilov, L. M. Plyasova, I. Y. Molina, G. A. Tsirlina, E. R. Savinova, *J. Solid State Electrochem.* **2008**, *12*, 497–509; d) I. Muylaert, P. Van Der Voort, *Phys. Chem. Chem. Phys.* **2009**, *11*, 2826–2832; e) P. Kuhn, P. Pale, J. Sommer, B. Louis, *J. Phys. Chem. C* **2009**, *113*, 2903–2910; f) F. Zhou, A. Izgorodin,

R. K. Hocking, L. Spiccia, D. R. MacFarlane, *Adv. Energy Mater.* **2012**, *2*, 1013 – 1021; g) M. Cargnello, V. V. T. Doan-Nguyen, T. R. Gordon, R. E. Diaz, E. A. Stach, R. J. Gorte, P. Fornasiero, C. B. Murray, *Science* **2013**, *341*, 771 – 773; h) A. G. Oshchepkov, A. N. Simonov, P. A. Simonov, A. N. Shmakov, N. A. Rudina, A. V. Ishchenko, O. V. Cherstiouk, V. N. Parmon, *J. Electroanal. Chem.* **2014**, *729*, 34 – 42; i) A. N. Simonov, O. V. Cherstiouk, S. Y. Vassiliev, V. I. Zaikovskii, A. Y. Filatov, N. A. Rudina, E. R. Savinova, G. A. Tsirlina, *Electrochim. Acta* **2014**, *150*, 279 – 289; j) H. J. King, S. A. Bonke, S. L. Y. Chang, L. Spiccia, B. Johannessen, R. K. Hocking, *ChemCatChem* **2017**, *9*, 511 – 521.

[18] a) B. M. Hunter, H. B. Gray, A. M. Müller, *Chem. Rev.* **2016**, *116*, 14120 – 14136; b) I. Zaharieva, D. Gonzalez-Flores, B. Asfari, C. Pasquini, M. R. Mohammadi, K. Klingan, I. Zizak, S. Loos, P. Chernev, H. Dau, *Energy Environ. Sci.* **2016**, *9*, 2433 – 2443.

[19] S. A. Bonke, A. M. Bond, L. Spiccia, A. N. Simonov, *J. Am. Chem. Soc.* **2016**, *138*, 16095 – 16104.

[20] R. A. Scott, J. E. Hahn, S. Doniach, H. C. Freeman, K. O. Hodgson, *J. Am. Chem. Soc.* **1982**, *104*, 5364 – 5369.

[21] A. Tenderholt, B. Hedman, K. O. Hodgson, in *XAFS13, Vol. 882*, AIP, Stanford California, **2007**, pp. 105 – 107.

[22] *MicroSoft Excel*, **2007**.

[23] B. Ravel, M. Newville, *J. Synchrotron Radiat.* **2005**, *12*, 537 – 541.

Manuscript received: June 6, 2017

Accepted manuscript online: July 18, 2017

Version of record online: August 28, 2017